DOI 10.4430/bgo00413

A two-step screening procedure to identify zones with higher hydrocarbon potential in a sandstone reservoir using geomechanical parameters

Y. Taras and M.A. Riahi

Institute of Geophysics, University of Tehran, Iran

(Received: 5 June 2022; accepted: 6 January 2023; published online: 22 March 2023)

ABSTRACT The main objective of this study is to discriminate high-potential hydrocarbon zones utilising a two-step screening procedure on three-dimensional pre-stack seismic data accompanied by information from four wells. In the first step, we prepared an integrated attribute consisting of P-wave impedance (Z_P), V_P/V_S, Young's modulus (*E*), Poisson's ratio (*v*), and Mu-Rho (*MR*) geomechanical parameters. By performing simultaneous inversion, acoustic impedances, and density were obtained. Then, the geomechanical parameters were extracted using several equations. To identify and assess zones with high hydrocarbon potential, the integrated attribute was accomplished laterally and vertically at the various zones of a reservoir layer. We found that when a lower value of the integrated attribute appears at a higher thickness of the reservoir layer, it indicates the zones with higher hydrocarbon potential. In the second step, to single out the shale, brine, and hydrocarbon-bearing intervals, the high hydrocarbon potential locations identified in the first step were used and five scatter plots were prepared. The scatter plots consist of *E* versus *v*, Z_P versus V_P/V_S, Z_P versus *v*, *MR* versus Lambda-Rho (*LR*), and *MR*/*LR* versus *LR*. Among them, the *MR*/*LR* versus *LR* and Z_P versus *v* best-distinguished shale, brine, oil, and gas-bearing intervals.

Key words: geomechanical parameters, hydrocarbon potential, integrated attribute, the screening procedure.

1. Introduction

A question that may come into the reader's mind is: why is the screening word used in this study and why is the screening procedure important? The answer is that screening and evaluating an application is how the procedure can verify the results. Therefore, the screening procedure was performed to identify and assess zones with a suitable potential for hydrocarbon, as well as to distinguish between fluid contents along with the reservoir layer.

Reliable information on the geomechanical parameters of a hydrocarbon reservoir can play a key role during drilling operations. Geomechanics is an important issue in wellbore stability analysis, pore pressure evaluation, and reservoir investigation. The application of seismic data in hydrocarbon reservoirs can be divided into two main categories (Faraji *et al.*, 2017). The first category is related to reservoir modelling in identifying the distribution of subsurface properties such as structural and facies analysis (Kadkhodaie-Ilkhchi *et al.*, 2010). Secondly, some seismic attributes show a meaningful relationship that forms the basis of the extraction of different geological parameters (Na'imi *et al.*, 2014). The scope of this research falls into the second

category. Many attempts have already been put forward in this regard to derive lithology and fluid properties from seismic data (Omudo and Ebeniro, 2005; Ujuanbi *et al*., 2008; Pelletier, 2009).

Accurate estimates of the elastic and geomechanical characteristics of reservoir rocks are required for many types of design and implementation used in various applications such as drilling, geothermal energy, and geotechnical engineering (Nakaten *et al*., 2014). Failure to do so causes wellbore instability and problems such as collapse, kick, wash-out, or tightening, increasing drilling costs, stopping production, and, eventually, might indeed cause well loss (Das and Chatterjee, 2017). The accuracy of geomechanical parameters is particularly useful in obtaining subsurface information on formation properties and interpretating seismic data and reservoir characteristics (Li *et al*., 2018; Guo and Wang, 2019; Mandal and Ghosh, 2020).

Thus, there have been very many attempts in this regard. One of the useful rock attributes, in this case, is acoustic impedance. This attribute is commonly used as an important predictor for evaluating rock characteristics and facilitating stratigraphic interpretation in geophysical studies (Li *et al*., 2018). Morozov and Ma (2009) used well log calibration to improve the generation of acoustic impedance from seismic data. Bjorlykke *et al*. (2015) estimated pore pressure in the Gulf of Mexico using acoustic impedance based on seismic data.

In various studies, elastic moduli were used as geomechanical parameters. Perez (2010, 2011) examined reservoir geomechanical parameters using elastic moduli, such as Young's modulus (E), Poisson's ratio (ν), or Lamé parameters [Lambda (λ) and Mu (μ)]. Schön (2015) utilised ν to calculate fracture start pressure, and fracture closure pressure, and estimate the extent of hydraulic fractures as well. From seismic data, the dynamic E and ν show lateral fluctuations in elastic moduli and brittleness related to wellbore stability and fractured zones (Das and Chatterjee, 2018; Yasin *et al*., 2020).

Using other attributes, Khatibi *et al*. (2018) assessed the Single-Parameter Parabolic failure criterion using uniaxial compressive strength (UCS) from triaxial tests and a geomechanical model in one of the Persian Gulf fields, in Iran. Han *et al*. (2019) established an advanced study of wellbore stability in naturally fractured rocks by providing three key steps for the measurement of elastic parameters. Radwan *et al*. (2019, 2020, 2021) investigated pore pressure and fracture gradients using a variety of data and methods. They also carried out reservoir geomechanical modelling to analyse *in situ* stress and its relationship with reservoir properties such as depletion, production, and wellbore stability (Radwan and Sen, 2021; Radwan *et al*., 2021). Bagheri *et al*. (2021) provided a geomechanical model and wellbore stability analysis in a carbonate reservoir using acoustic impedance and reflection coefficient. They first used geomechanical modelling to evaluate the wellbore's stability and the safe mud window and, then, validated the geomechanical model using the acoustic impedance and reflection coefficient parameters. Kassem *et al*. (2021) calculated the geomechanical parameters to investigate the effect of depletion and fluid injection in a sandstone reservoir. Hoseinpour and Riahi (2021) used a compressional wave velocity log to determine geomechanical characteristics and a sonic log to measure V_P and V_S.

The quantity of geomechanical parameters can be obtained from the experiments on the cores. However, this approach is very expensive and time-consuming. It is also likely that cores are not accessible in all wells or at all depths within the well (Kong *et al*., 2019). Using well logs is a faster and less expensive method to calculate rock elastic parameters dynamically (Bagheri *et al*., 2021). As a result, the geomechanical parameters are typically calculated indirectly. Therefore, applicable terms can be obtained from seismic waves and elasticity moduli equations (Fjær *et al*., 2008).

In some investigations, a combination of wave velocity diagrams with the density (ρ) log makes it possible to estimate elasticity constants, and mechanical properties within the wellbore used (Soleimani *et al*., 2018; Khoshnevis-zadeh *et al*., 2019). Several of these attempts were using VSP

(vertical seismic profile) data. According to Rutqvist *et al*. (2009), VSP can be used to predict *v* and *E*. It can also be used to determine the velocity of the waves in different layers and compare them to the sound logs (Hackert and Parra, 2002; Yang *et al*., 2020). The saturation changes and types of fluid in the rock pores can be determined by the quality factor (*Q*) (Khaitan *et al*., 2017; Lu *et al*., 2018; Shahbazi *et al*., 2020). Larki *et al*. (2021) investigated *Q* frequency content using VSP data for gas reservoirs. They studied the relation between quality factors and porosity and introduced it as an indicator of high porosity ranges. It was deduced that the frequency range changes according to the amount of gas. So, they concluded that if VSP data are available for a well, it is possible to estimate the amount of gas abundance by considering its frequency range regardless of the type of rock and just with the help of frequency analysis of *Q*. Larki *et al*. (2021) employed the K-Mean clustering approach to cluster geomechanical characteristics and determine geomechanical units. This method can determine the possible zones for hydraulic fracturing by analysing and comparing the velocity deviation log (VDL) and UCS. They used VSP and petrophysical logs to generate a geomechanics-integrated model of the formation rock. Then, using this geomechanical model, key concepts like the safe mud window and the hydraulic fracture potential were verified by the VDL information.

However, there are large uncertainties and limitations in the current common methods for the determination of geomechanical parameters (Matsushima *et al*., 2016; Khaitan *et al*., 2017; Wu *et al*., 2017). According to the above explanations, there are three basic issues regarding the previous studies. First, most of these studies use a single attribute analysis. But in general, the researchers found that no single attribute provides enough information to correlate seismic data with reservoir properties (Bathellier *et al*., 2012). Second, the VSP surveying method and the core analysis are expensive and they are limited to certain locations or wells. By using seismic data, these parameters can be calculated in a wide range of areas, thus minimising the cost and risk of the drilling operation. Third, most of the mentioned investigation methods are time-consuming, so we are looking for a procedure able to give us an accurate assessment of the reservoir's hydrocarbon potential quickly. In the current paper, we consider a two-step screening procedure to assess the reservoir layer in identifying zones with a suitable hydrocarbon potential as well as distinguish between shale and zones containing various fluid contents. In the first step, an integrated attribute consisting of five geomechanical parameters is performed to screen and assess laterally the different locations of a reservoir layer and identify suitable hydrocarbon potential; then, the suitable locations will be screened and evaluated vertically. The scatter plots were performed to determine whether or not every two geomechanical parameters have a relationship or correlation. Therefore, to distinguish between shale and fluid contents of the suitable locations identified in the first step, five scatter plots were used. The plots include *E* versus *v*, P-wave impedance (Z_P) versus V_P/V_S, Z_P versus *v*, Mu-Rho versus Lambda-Rho (*LMR*), and Mu-Rho/Lambda-Rho versus Lambda-Rho will be performed and screened in the second step. This study's importance is finding a method to achieve the mentioned issues. Hence, by examining the results of previous researchers, the most effective parameters were used in the design of the 'integrated attribute' and the scatter plots. This procedure can be highly useful in the petroleum industry.

2. Study area and geology

The study area is one of the hydrocarbon fields in the NW of the South Pars. The reservoir consists of resedimented sands belonging to the Arabian Shield (Hejaz igneous shield), which

has been mixed with low-metamorphic sandstones and deposited in a relatively energetic environment near the shore during the Oligo-Miocene forward-backward sequence (Koop and Stoneley, 1982; Alsharhan and Nairn, 1997). The thickness of the reservoir layer in this area reaches a maximum of 100 m. It is made up of non-dense sandstone of Ahvaz, shale, and dolomite. Therefore, the upper part contains flowing sand and in the lower part, these sands are connected by carbonate cement. The total porosity and the effective porosity are almost equal in most parts of the reservoir and this may be due to the low volume of shale. In addition, porosity changes are not high at the reservoir horizon and it has acceptable useful porosity as a hydrocarbon reservoir (James and Wynd, 1965).

3. Methodology

3.1. Geomechanical parameters

The application of geomechanics in different disciplines of the petroleum industry, such as hydraulic fracturing, subsurface gas storage, fault reactivation, variation in permeability trends, and oil production, is well known (Faraji *et al*., 2017). Geomechanical properties play an important role in field development phases from drilling to production stages. Accordingly, even approximate knowledge about these rock properties is crucial (Zoback, 2007).

A mechanical Earth model (MEM) is a quantitative description of rock mechanical properties in the subsurface. MEMs could be one-dimensional (built from well-logs) or three-dimensional (built from 3D seismic inversion). Most MEMs are one-dimensional. The concept of using 3D seismic data to extend the MEM to 3D space was introduced a few years ago. The five major components of a MEM are (Sengupta *et al*., 2011):

1. structural model consisting of surfaces and faults from seismic data;
2. lithology (including the fractions of the mineral components and porosity);
3. elastic properties (such as v, shear modulus, E, Bulk modulus, etc.);
4. rock strength (such as compressive and tensile strength);
5. *in-situ* stresses (such as overburden stress and pore pressure).

In this study, we mostly investigate elastic properties in 3D space.

3.2. Overview of available data

Available information is well logs and 3D pre-stack seismic data. There are four active wells in the area. Well logs consist of sonic, ρ, and check-shots. There were two reasons for choosing these wells. First, they have a suitable distribution in the study area. Second, more well logs were available from the mentioned wells.

3.3. Experimental data

A 2D sample cross-line number 1679 seismic section from the studied 3D seismic data is shown in Fig. 1.

3.4. Theoretical concepts

Accurate delineation and assessment of the quality of hydrocarbon reservoirs are vital for the development of well planning to reduce risks in selecting new drilling locations (Adeoti *et al*.,

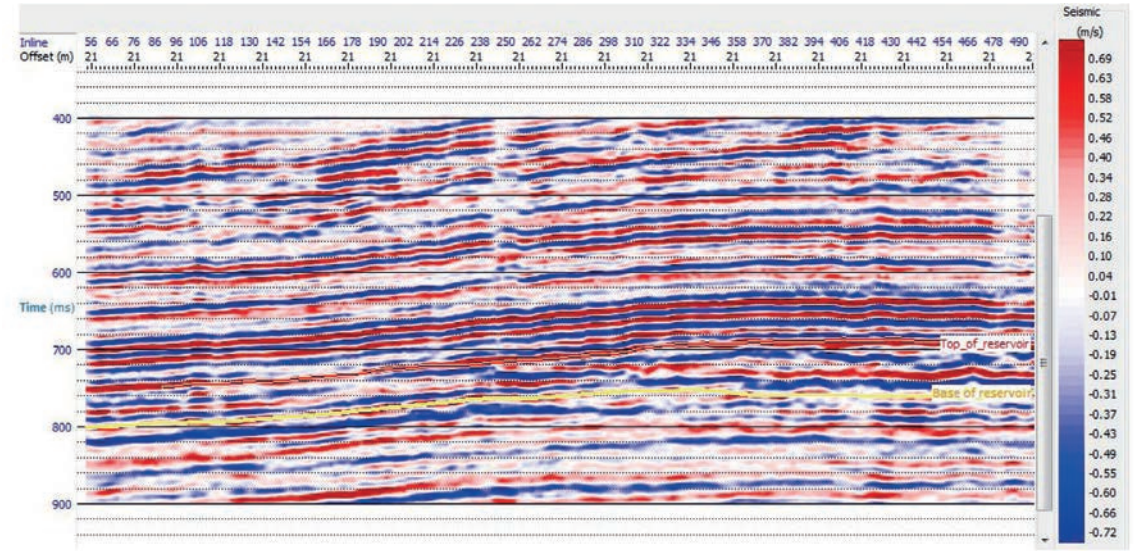

Fig. 1 - A 2D cross-line number 1679 seismic section from the 3D seismic data. The full 3D data cube used in this study contains 280 in-lines and 300 cross-lines. The cross-line number 1679 is shown as sample data from the studied 3D cube. The top and the base of the reservoir layer are marked in this figure.

2018). This would require the integration of seismic and well data to enhance vertical and lateral resolution (Suslick *et al*., 2009).

Determining the elastic parameters inversion process of seismic data involves two main steps:

1. estimation of reflectivity as a function of incidence angle at each reflection boundary in the subsurface;
2. inversion of the reflectivity to estimate the corresponding elastic parameters by some mathematical models (Adesanya *et al*., 2021).

In the inversion stage, the Zeoppritz equations were used based on Aki and Richards (1980) approximation for PP and PS data.

3.5. Simultaneous inversion

Simultaneous inversion of seismic data is capable of converting several angle stacks to elastic parameters, which are capable of distinguishing lithology and pore fluids within the reservoirs (Goodway, 2001). Pre-stack simultaneous inversion estimates Z_P, S-wave impedance (Z_S), and ρ, which in turn can be used to predict lithology and geomechanical properties (Goodway, 2001). In this case, first, we transform seismic data to angle gathers as shown in Fig. 2.

Then, we estimated the Z_P and Z_S from the inversion algorithm and, finally, we estimated the Lame parameters (λ and μ). One of the most important steps to conduct the inversion is the first arrival picking because the slightest error in this step causes a large difference in results (Soleimani *et al*. 2018). According to Akram and Eaton (2016), there is an urgent need for automatic picking methods as the scale of seismic data continues to grow. There are three main types of first-arrival picking methods. The first and the most common is Coppens' method (Coppens, 1985). It uses energy ratios within two amplitude windows to process the data. The second is the direct correlation method (Molyneux and Schmitt, 1999). It uses the maximum cross-correlation value as a criterion, which fails in data sets with a low signal-to-noise ratio. The third is the back-propagation neural networks method (McCormack *et al*., 1993). It applies

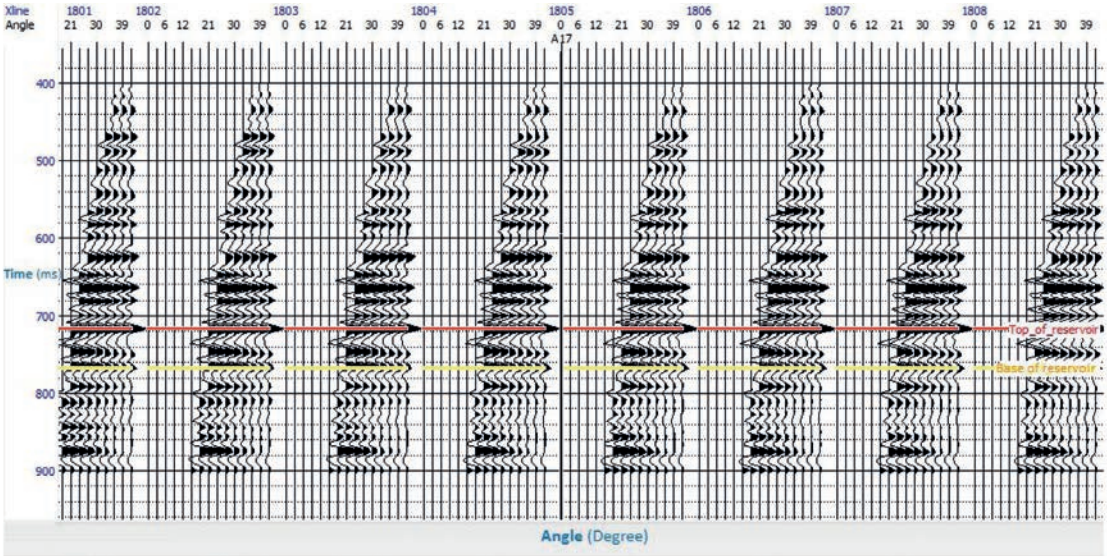

Fig. 2 - Created angle gathers from the in-line 250 pre-stack seismic data using well logs in different CDPs. The maximum angle of incident is 40° in this study. These angle gathers are performed using 20 angle bins from 0° to 40°. The velocity model extracted from existing well logs was used to perform these angle gathers.

back-propagation neural networks in first-arrival refraction event picking and seismic data trace editing. Many researchers have developed these methods over the years. However, the use of automatic methods alone, especially when the signal-to-noise ratio is low, can be accompanied by errors. Therefore, in this research, we used a combination of manual and automatic methods to increase accuracy. This means that the results of the automatic method were modified manually. We used the single-trace boundary detection algorithm, which is more noise-resistant. It can be described as follows (Pan *et al*., 2019):

$$S_i = |(B / A) \times (B - A)| \tag{1}$$

where:

$$A = \sum_{p=i}^{p=i-n} S_{p,} \qquad B = \sum_{p=i}^{p=i+n} S_p$$

Here, S_i is the boundary characteristic value of the first arrival obtained for the *i*th sample point; S_p is the amplitude of the *p*th point of a seismic trace. *A* is the sum of the amplitudes of *n* points before the current point in the same trace and *B* is the sum of the amplitudes of *n* points after the current point in the same trace. Before performing the inversion process, the correlation between the seismic trace and the synthetic trace was estimated to ensure the proper accuracy of the steps performed. As shown in Fig. 3, the correlation coefficient with an accuracy rate of 0.99% was obtained; which indicates a high accuracy in performing the inversion process.

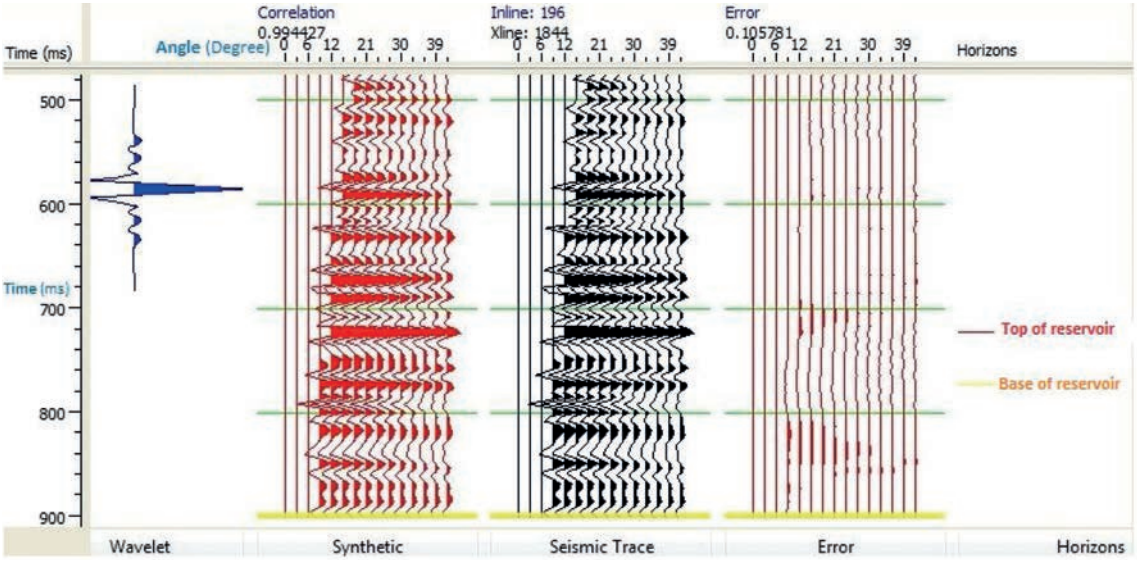

Fig. 3 - Correlation between real seismic and synthetic traces. The wavelet used in the inversion process is shown in the left column. To avoid the influence of inaccurate wavelet phase estimation on seismic inversion, several wavelets were extracted statistically based on wellbores information. Finally, an accurate statistical wavelet was chosen with less error in the inversion process. The correlation coefficient obtained between synthetic and seismic traces is about 0.99% and the error is 0.105781. Ultimately, the location of seismic horizons matches well with the real seismic trace and synthetic trace.

The inversion process results, including Z_P, Z_S, and ρ, are shown in Figs. 4a, 4b, and 4c. Other reservoir properties including geomechanical parameters are derived from these results. The geomechanical parameters used in this research are described in the following sections.

4. Elastic modulus estimation

The estimation of elastic modulus plays a very important role in the precise estimation of reservoir properties. The estimated elastic moduli in this research are as follows.

4.1. Poisson's ratio

This ratio helps to verify the brittleness of a reservoir horizon, distinguishing the clean sand of the reservoir from the shaly sand zone and identifying the reservoir fluids. v can be estimated in two approaches. The first method is using the velocity of P and S waves. This method is more common and has more history in scientific research. The way it is estimated is as follows:

$$v = (V_P^2 - 2V_S^2)/(2V_P^2 - 2V_S^2) \quad (2)$$

Eq. 2 is based on the velocity of the seismic waves. Seismic velocity is prone to a certain amount of uncertainty and error, so using Eq. 2 in estimating v also is prone to error. Therefore, we estimate v merely based on P and S acoustic impedances obtained from the inversion process.

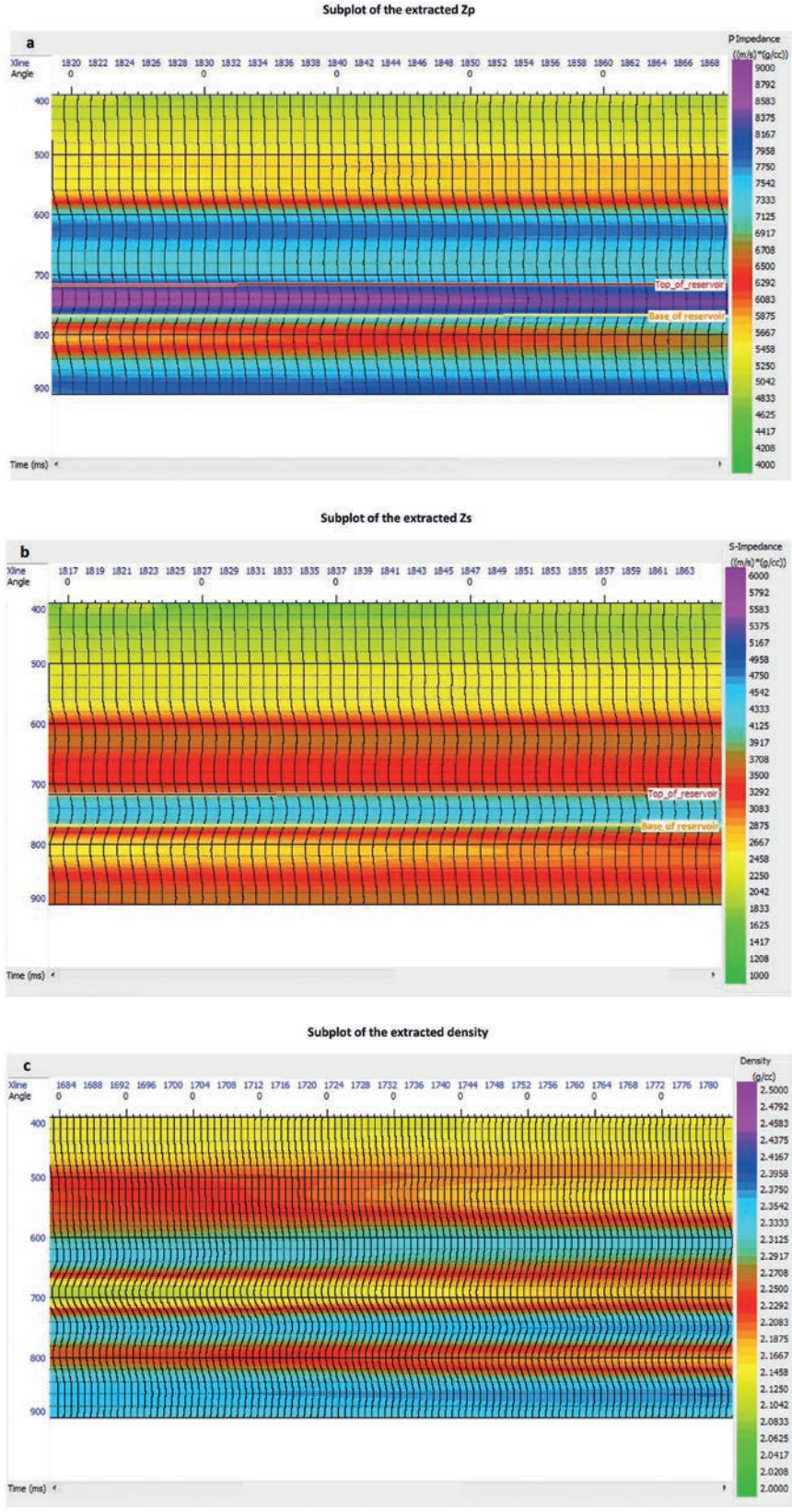

Fig. 4 - Subplots of the extracted Z_p (a), Z_s (b), and ρ (c). The inversion process was performed for the whole 3D data set. Here is an example of the obtained results for in-line 250. The top and the bottom of the reservoir are indicated in panels a and b. The top and bottom of the reservoir horizon are marked based on existing wellbores' check shots in the area of study.

We estimated *v* without using the seismic velocity as follows. Multiplying the numerator and denominator of Eq. 2 by the squared *ρ*, we transform the above equation in terms of acoustic impedance (*I*) as follows:

$$v = (I_P^2 - 2I_S^2)/(2I_P^2 - 2I_S^2) \tag{3}$$

Thus, *v* is estimated accurately by taking into account the acoustic impedances without using the seismic velocity.

4.2. Young's modulus

E also has a high impact on determining the brittleness as well as the geology properties of the reservoir (identification of clean sands from shaly sand intervals) and singling out of the reservoir's fluid contents. The conventional way to calculate *E* is as follows:

$$E = \rho V_S^2 \times [(3V_P^2 - 4V_S^2)/(V_P^2 - V_S^2)]. \tag{4}$$

As can be seen, similar to the *v*, to calculate *E*, we need the P- and S-wave velocity and also *ρ*. Following the findings of Sharma and Chopra (2012), the computation of *E* from seismic data requires the availability of *ρ*. The computation of *ρ* in turn requires long offset seismic data, which are usually not available.

On the other hand, since in reservoir characterisations, two important parameters are *ρ* and *E*, we are looking for a parameter that can include both of them at the same time, and also it should be estimated merely based on acoustic impedance. Sharma and Chopra (2012) suggested the product of *ρ* multiplied by *E* leads to such purpose. Eq. 4 is based on *ρ* and velocity. Multiplying the numerator and denominator of each item in the bracket by squared *ρ*, then multiplying the left and right of Eq. 4 by the *ρ*, a purely acoustic impedance-based equation will be obtained.

This equation is as follows:

$$E \times \rho = I_S^2 \times [(3I_P^2 - 4I_S^2)/(I_P^2 - I_S^2)] \tag{5}$$

4.3. Lambda-Rho

Lambda (*λ*), or the first Lame parameter, is a P-wave-derived parameter known as incompressibility. Since fluid contributes a reasonable amount to the total resistance exerted by a rock to compression, a change in fluid type and saturation amount is important in determining the incompressibility of a rock type. A systematic change in fluid type from brine to oil and then to gas will lead to a significant gradual reduction in the incompressibility of a rock (Ogbamikhumi and Igbinigie, 2020). Its multiplication to *ρ* (Lambda-Rho, *LR*) is more useful, which can be calculated as follows:

$$LR = Z_P^2 - 2Z_S^2. \tag{6}$$

LR can also be derived from P-impedance and V_P/V_S:

$$LR = Z_P^2 - 2[Z_P^2/(V_P/V_S)^2]. \quad (7)$$

4.4. Mu-Rho

Mu (μ), or the second Lame parameter, is a P-wave-derived parameter known as rigidity. It is expected to have a higher value in the sand than in the shale since the sand matrix exerts greater resistance to shearing than the shale matrix does. Its value is not affected by the nature and type of fluid content in the pore spaces. Hence, the value for the brine and hydrocarbon-filled sand is expected to remain relatively constant. Therefore, *MR*, which is its product with bulk ρ is a proper lithology indicator with high values indicative of sand (Goodway *et al*., 1997). It can be derived from Z_S as follow:

$$MR = Z_S^2. \quad (8)$$

Alternatively, using Z_P and V_P/V_S:

$$MR = Z_P^2/(V_P/V_S)^2. \quad (9)$$

In this study, we have attempted to minimise uncertainties and systematic errors in necessary parameter calculation. Therefore, we directly use the values of impedances instead of velocity. In this research, Eqs. 6 and 8 were used to estimate *MR* and *LR*.

5. Discussion

5.1. A two-step screening approach

An attempt was made to propose an efficient and reliable approach to distinguish and evaluate suitable locations of the hydrocarbon potential along with a reservoir horizon. To meet this objective, the geomechanical parameters along with the reservoir horizon were estimated. Then, by an appropriate combination of the estimated geomechanical parameters, an integrated attribute was achieved, and a two-step screening approach was proposed:

- Step 1: in this step, an integrated attribute is provided consisting of the Z_P, V_P/V_S, v, E, and *MR* geomechanical parameters. Then, to identify hydrocarbon potential along with the reservoir horizon, a screening balance was established between the integrated attribute value and the thickness of the reservoir horizon;
- Step 2: in this step, to distinguish between the brine, hydrocarbon, and shale zones, the high hydrocarbon potential locations are screened and identified in the first step and will be used as input to perform five scatter plots. The scatter plots, consist of E versus v, Z_P versus V_P/V_S, Z_P versus v, *MR* versus *LR* (*LMR*), and *MR*/*LR* versus *LR* were performed. The workflow illustrating the stages involved in the two-step screening procedure is presented in Fig. 5. According to the above explanations, for the appropriate screening using different geomechanical parameters, the information in Table 1 is used.

Table 1 - The relationship between seven effective geomechanical parameters with geology and fluid is classified in this table. The resolution of different parameters is different from each other. For example, the parameter *MR* would not distinguish between pore fluids and can only separate shale and sand. In this research, by plotting different cross-plots, we compare their performance.

The relationship between seven effective geomechanical parameters with geology and fluid.							
M/L unit less	***LR* Gpa × (g/cc)**	***MR* Gpa × (g/cc)**	***v* unit less**	***E* N/m²**	***VP/VS* unit less**	**P-impedance (m/s) × (g/cc)**	**Parameter/ Lithology**
Very high	Very high	Low	Very high	High	High	Very high	Shale
Low	Low	Higher than	Low	Low	Low	Low	Brine sand
		shale					
Very low	Very low	Same as brine	Very low	Very low	Very low	Very low	Oil sand
Much lower	Much lower	Same as brine	Much lower	Much lower	Much lower	Much lower	Gas sand

5.2. Step 1 - Calculating integrated attribute, the thickness of the reservoir layer, and selecting the best location in terms of hydrocarbon potential

In the first step, first, we calculate the 'integrated attribute' by combining five different geomechanical parameters along with the reservoir layer consisting of P-impedance, V_P/V_S, v, E, and MR. Then, we calculate the thickness along with the reservoir layer and plot it as a horizontal slice. Finally, by creating a balance between the least amount of 'integrated attribute' and the maximum amount of thickness of the reservoir layer, we select the best location in terms of hydrocarbon potential.

Since in calculating the integrated attribute in the software, the product of multiplying several slices is used, we use the word 'horizontal slice' for this. But in calculating the thickness of the reservoir layer, the difference between the depth of the upper and lower horizons of the reservoir is used, and, therefore, we introduce it with the term 'horizontal map'.

5.2.1. Integrated attribute

According to the explanation of the previous section, P-impedance, V_P/V_S, E, v, and MR values have lower values for hydrocarbon sand compared to brine sand and shale, respectively. Therefore, by combining all the above parameters and obtaining a single output, and plotting this output in a 'horizontal slice' for the entire reservoir, three important goals can be pursued. First, by having a 'horizontal slice' for this single output, it is possible to make a fast separation between different parts of the reservoir. Second, by combining the parameters, the effect of errors in each of the parameters can be minimised and somewhat eliminated. Thirdly, by multiplying these parameters together and enlarging the output numbers, we can increase the resolution between the high and low values of the output map and this simplifies the detection of the smallest values. We then introduce the final parameter designed to create the output slice as an 'integrated attribute' and calculate it as follows:

$$\text{Integrated attribute} = \text{P-impedance} \times V_P/V_S \times E \times v \times MR. \quad (10)$$

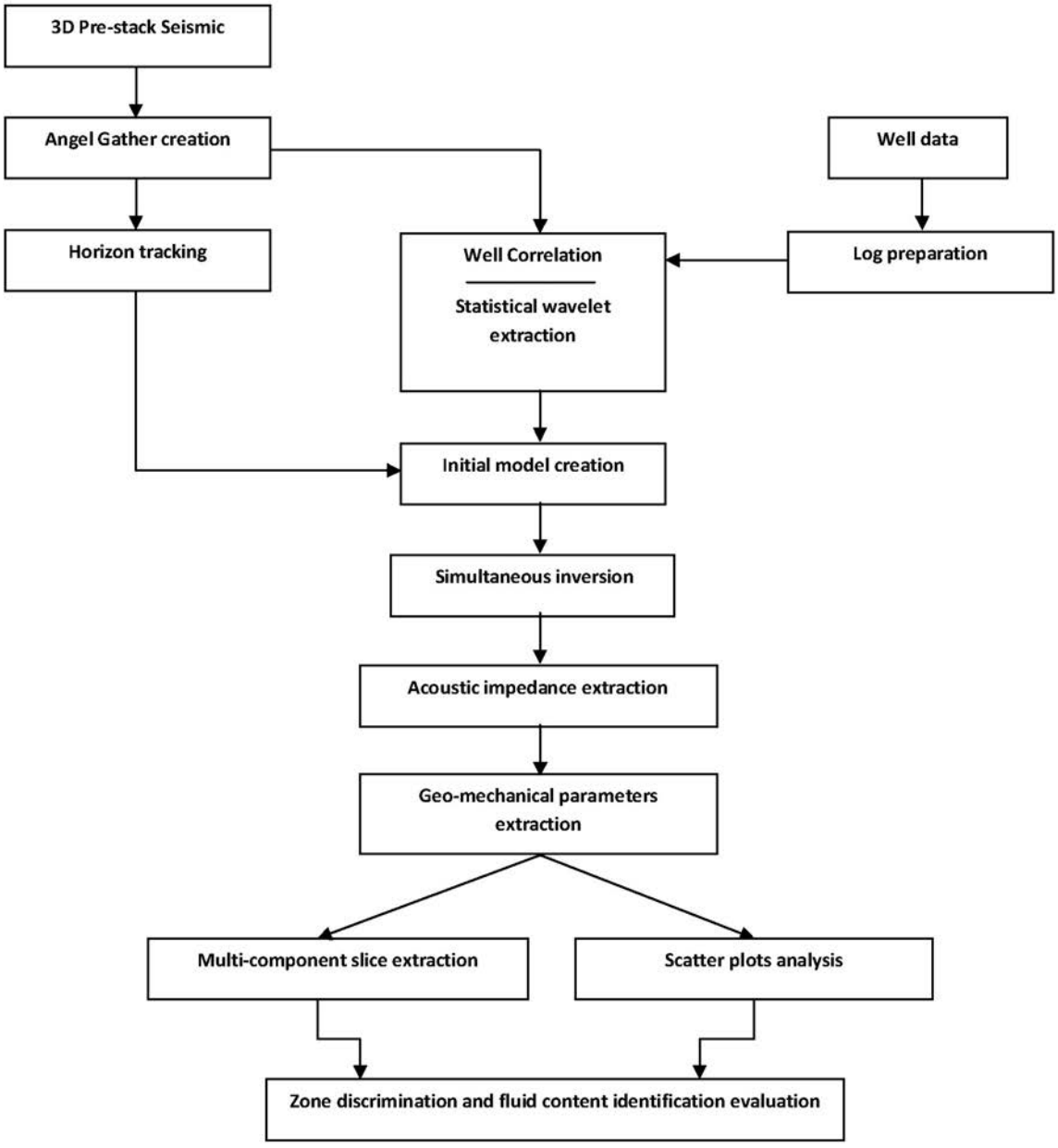

Fig. 5 - The workflow illustrates the stages involved in the two-step screening procedure. Based on this workflow, first, the simultaneous inversion is performed. The results are Z_p and Z_S and ρ. Using these results, the geomechanical parameters such as Lame parameters, elastic modulus, and brittleness were calculated. The multi-component slice is part of the data that passes through the reservoir layer. The parameter used in this slice is named 'integrated attribute', which is the combination of five geomechanical parameters. Then, by using the performed two-step screening procedure, an evaluation of geology and fluid content in the reservoir could be assessed. Furthermore, the shale zone was distinguished from the hydrocarbon content in the sandstone along with the reservoir layer.

We calculate the value of the 'integrated attribute' using Eq. 10 for the horizontal slice that passes through the middle of the reservoir layer. Fig. 6 shows the output horizontal slice. According to this figure, the lowest 'integrated attribute' belongs to wells B, A, C, and D, respectively.

5.2.2. Thickness

In the previous sections, the main reservoir layer was plotted in the whole area, using existing well data and the upper and lower horizons of the reservoir layer. Areas that are thicker in the reservoir area can have a better potential for hydrocarbon extraction. Therefore, we consider the thickness of the reservoir layer as an important parameter in identifying the best locations of the hydrocarbon reservoir and plot a horizontal map of the thickness of the reservoir layer. This map is shown in Fig. 7: according to this figure, the thickest reservoir layer is related to wells A, C, D, and B, respectively.

5.2.3. Selected location

In this research, we select a location that has a greater reservoir layer thickness and also a lower integrated attribute value as the 'selected location' and uses it in the second step. It should be noted that to select this location, a balance must be established between the integrated attribute and the thickness of the reservoir layer. Because a location that has the least amount of the integrated attribute does not necessarily have the maximum thickness and vice versa.

Regarding these assumptions, the position of the selected location is chosen and shown in Figs. 6 and 7.

5.3. Step 2: Elastic properties and scatter plot analysis

In the second step, we evaluate the selected location (Figs. 6 and 7) obtained from the first step vertically. By plotting several scatter plots for the selected location, we examine it in-depth and separate its hydrocarbon and shale ranges.

Scatter plotting is a graphical representation of the plot of two or more rock properties. It aids in the easy and meaningful evaluation of these rock properties (Castagna and Swan, 1997). Scatter plots are one of the best tools for distinguishing between sandstone and shale as well as reservoir fluid detection. The advantage of the scatter plot is now a commonly used technique in rock physics analysis as it allows for a fast and more meaningful evaluation of attributes (Castagna and Swan, 1997). Generally, the majority of the common lithology units and fluid types tend to form separate clusters in cross-plot and this helps in making a direct interpretation (Omudo and Ebeniro, 2005). Goodway *et al*. (1997) suggested four rock attributes derived from seismic inversion for lithology and pore fluid discrimination: V_P/V_S and ν, Lambda-modulus, and ρ, shear rigidity and ρ, and Z_P. They demonstrated that Lame's parameters (*LR* and *MR*) could be good pore fluid and lithology indicators, respectively.

We use the most appropriate combination of geomechanical parameters in drawing cross-plots. It should be noted that scatter plots are usually drawn using data from wells, but we use the seismic data from the screened locations in the previous step. The important point here is proper clustering between dots. With proper clustering, good results can be obtained in the field of geology assessment and fluid type detection. The cross-plots used in this research are divided into several categories that comprehensively assess the condition of the reservoir. The cross-plots used are given in the following sections.

In most of the similar studies that have been done before on scatter plots, proper separation of the dots related to the geomechanical parameters is insufficient owing to a lot of overlap between different clusters. Shuaib and Berguig (2022) tried to separate shale and sand using a P-impedance scatter plot, but the obtained clusters had relatively considerable overlap, and in addition, the separation was not very accurate. Larki *et al*. (2022) attempted to perform more

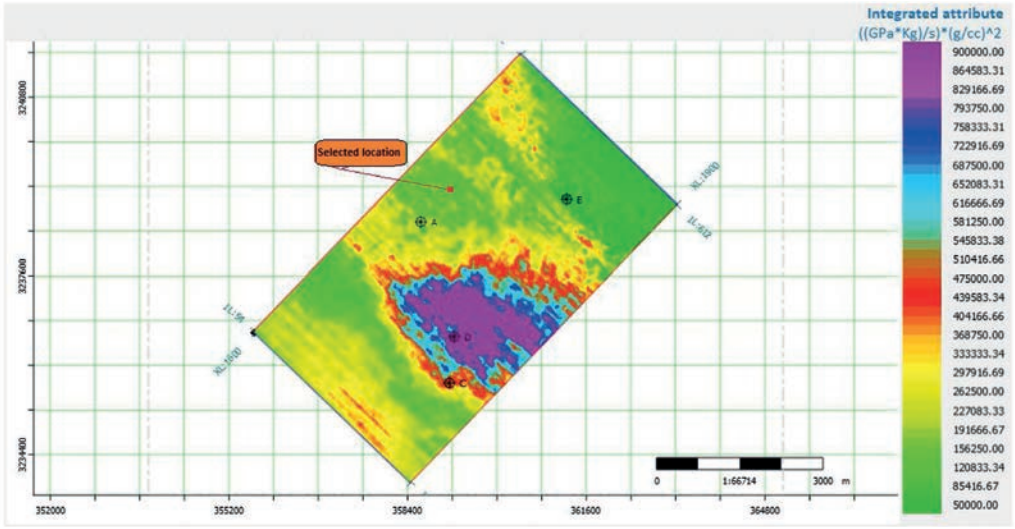

Fig. 6 - 'Horizontal slice' of the 'integrated attribute'. The integrated attribute is the product of five geomechanical parameters. The identified location with high potential hydrocarbon is marked as a selected location. This location is placed in the green area, which indicates a lower value of the integrated attribute.

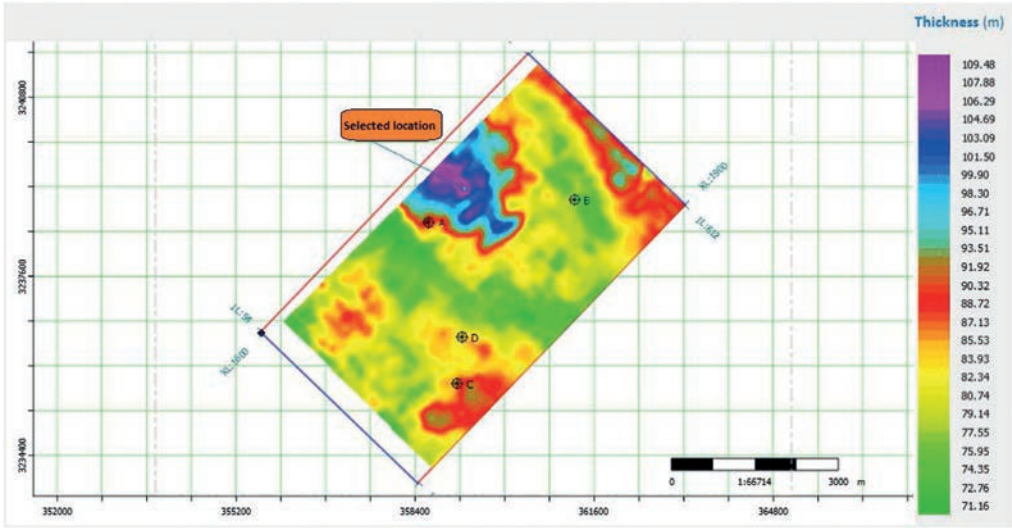

Fig. 7 - Thickness 'horizontal map'. The higher thickness is shown with the dark purple colour. A comparison with Fig. 5 indicates that the higher thickness of the reservoir horizon is compatible with the lower value integrated attribute value marked in Figs. 6 and 7 as the selected location with better hydrocarbon potential. Therefore, the dark purple colour range, which has the highest thickness, is chosen as a selected location of the reservoir horizon. In choosing the selected location, it should be noted that both the value of the 'integrated attribute' and the amount of thickness should be considered at the same time. Selecting the location based on just one item will not necessarily lead to a reliable result.

accurate clustering on scatter plots by applying robust boundaries for the minimum, maximum, and average of different geomechanical parameters like *E*, *v*, and the bulk modulus; also in this approach, the dots in the scatter plots were not completely separated from each other and, due to the application of robust boundaries, there was the possibility of some errors. These issues

could result from a large number of dots. According to the design of a two-step procedure in this research, the dots of the scatter plots are limited to a specific location. Therefore, the common problems regarding clustering are solved and the dots are separated from each other accurately.

5.3.1. Young's modulus versus Poisson's ratio

Based on the previous discussions, brittle and rich reservoir represents areas with low *v* and low *E*. With this assumption, we plot *E* versus the *v* for the selected location (Figs. 6 and 7). By clustering this cross-plot according to Fig. 8, the dots are divided into three categories. The dots with low values for the *E* and the *v*, clustered in red, are assumed to be hydrocarbon sands. Dots with average *E* values and average *v*, clustered in blue, are areas with brine sand, and dots that have high *E* values and a high *v* are clustered in green considered shale zone.

On the other hand, the colour bar at the right of Fig. 8 indicates time. As can be seen, the red dots (less time namely less depth) are in the hydrocarbon range, orange and green dots (medium time or depth) are in the brine sand range, and dark blue and purple dots (more time or depth) are in the shale range. Therefore, in this way, hydrocarbon and shale areas can be separated in terms of time (depth). It was thus observed that the sequence of layers is consistent with the geology of the area. This result is itself proof of clustering accuracy. Generally, in all cross-plots of this research, the clustering of dots has been done according to Table 2. Also, geomechanical specifications according to Fig. 8 are shown in Table 3.

5.3.2. P-impedance versus V_p/V_s

Following Datta Gupta *et al*. (2012) investigations, the hydrocarbon-bearing sands, exhibit lower V_p/V_s and relatively low P-impedance. Accordingly, the results obtained by plotting the cross-plot of the P-impedance versus V_p/V_s are shown in Fig. 9. As can be seen, similar to the previous cross-plot, the dots are clearly separated into three categories: red (hydrocarbon

Table 2 - The dots are clustered into 3 colours. The red cluster represents hydrocarbon sand, the blue cluster represents brine sand and the green cluster represents shale. In some cases, the separation between gas and oil is also possible. In this case, gas hydrocarbon is displayed in yellow and oil hydrocarbon is displayed in a red cluster.

Lithology and fluid clusters	
Lithology	**The background colour of the cluster**
Hydrocarbon sand	Red
Brine sand	Blue
Shale	Green

Table 3 - Geomechanical specifications according to Fig. 8.

Geomechanical specifications according to Fig. 8			
Geology/Fluid content	**ERho Gpa × (kg/m³)**	***v*** **Unit less**	**Colour of dots**
Shale	20000-100000	0.25-0.39	Green - blue - purple
Brine sand	10000-40000	0.24-0.36	Yellow - green
Hydrocarbon sand	10000-24000	0.13-0.28	Red - orange

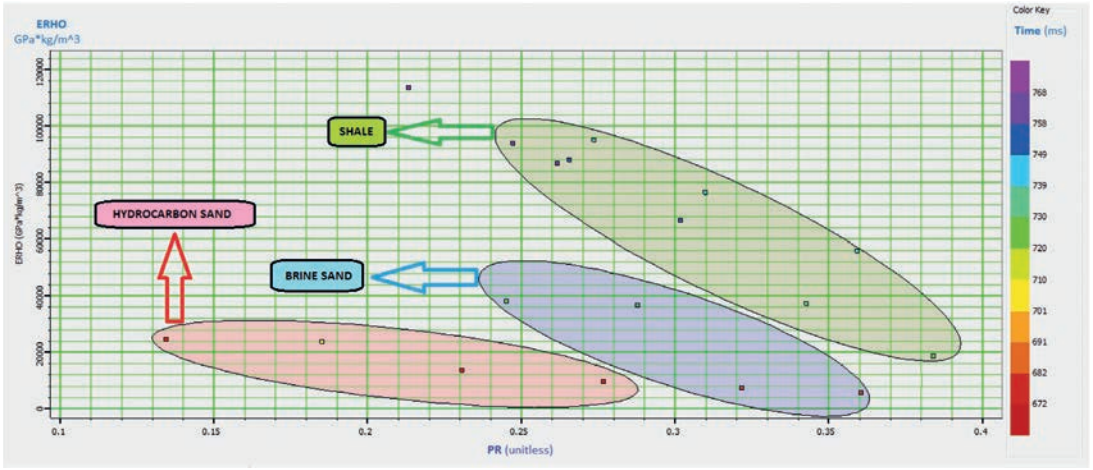

Fig. 8 - *E* versus *v* cross-plot for the selected location (Figs. 6 and 7). The dots are divided into 3 clusters. The red cluster includes mostly red dots, which have less depth and is attributed to hydrocarbon sand. The blue cluster includes orange and green dots, which have a moderate depth and is attributed to brine sand. The green cluster mostly includes dark blue and purple dots, so it has more depth and we assume it is shale. Most of the dots are located in the green cluster. One of the dots is not located in any of the clusters. Placing more dots inside the clusters indicates better performance of the scatter plot.

sand), blue (brine sand), and green (shale). Geomechanical specifications according to Fig. 9 are shown in Table 4.

5.3.3. P-impedance versus Poisson's ratio

The Poisson's ratio (*v*) distinguishes shale with a high value from brine sand with a lower value, and a much lower value will be observed for hydrocarbon-bearing sand. As we know,

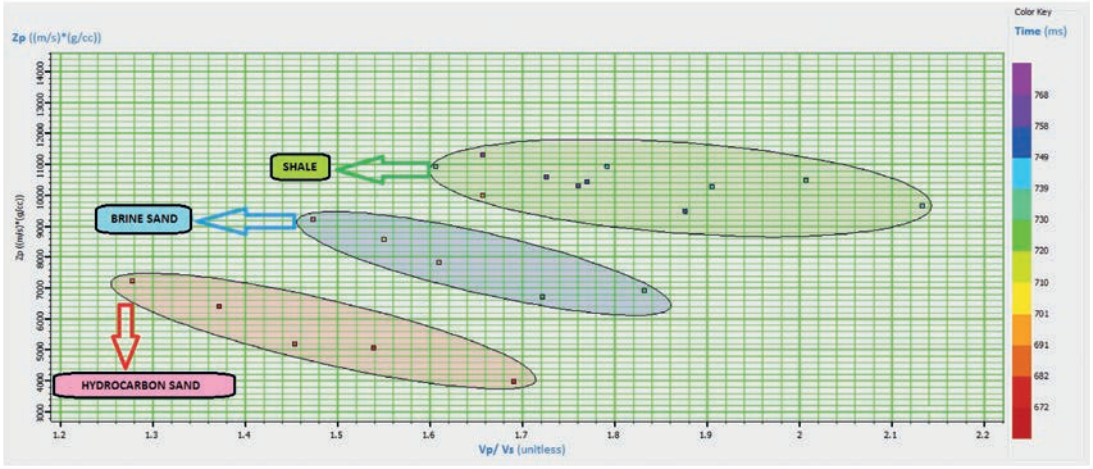

Fig. 9 - P-impedance versus V_P/V_S ratio cross-plot for the selected location (Figs. 6 and 7). The dots are divided into 3 clusters. The red cluster includes red dots belonging to less depth and we assume it is hydrocarbon sand. The blue cluster includes orange and green dots belonging to moderate depth and it is attributed to brine sand. The green cluster mostly includes dark blue and purple dots belonging to more depth. We assume it is shale. Here all of the dots are placed inside the clusters. This may somewhat indicate a better performance of this scatter plot than the previous one.

Table 4 - Geomechanical specifications according to Fig. 9.

Geomechanical specifications according to Fig. 9			
Geology/Fluid content	**Z_P (m/s) × (g/cc)**	**V_P/V_S Unit less**	**Colour of dots**
Shale	9500-11000	1.6-2.12	Green - blue- purple
Brine sand	7000-9500	1.46-1.84	Yellow - green
Hydrocarbon sand	4000-7000	1.28-1.7	Red - orange

Z_P is the product of P-wave velocity and ρ. Since P-wave velocity and ρ show similar behaviour in terms of decreasing values in the presence of hydrocarbon, the Z_P will therefore be further reduced in the presence of hydrocarbon and it is a very good indicator for hydrocarbon sand separation. Hence, a reduction is expected for a change from brine to oil, or from oil to gas. This scatter plot is a fluid indicator because P waves are sensitive to fluid variation, whereas S waves are not (Krebs *et al*., 2009). Thus, the P-impedance versus *v* cross-plot indicates a very high value of *v* and a relatively higher value of P-impedance defining shale lithology. Brine sand is defined by a very low value of *v* and a relatively lower value of P-impedance. The hydrocarbon is characterised by a relatively much lower value of P-impedance and a lower value than the brine-filled portion of the reservoir. The results of drawing this cross-plot are given in Fig. 10. In this case, the separation is much better than in other cross-plots, so we have added a new yellow clustering to this chart, possibly separating gas from oil. So, the gas carrier locations (red dots), which have less depth according to the colour bar are clustered with yellow colour and the oil locations (yellow and green dots), which have more depth than the gas carrier locations are clustered with red colour. The high resolution of this cross-plot makes it one of the best tools to get the desired results. Geomechanical specifications according to Fig. 10 are shown in Table 5.

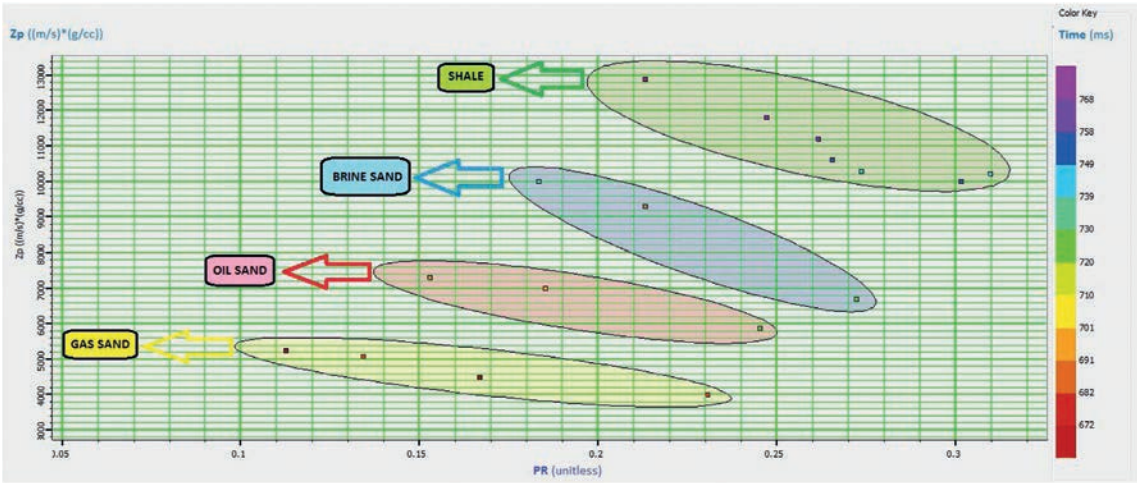

Fig. 10 - P-impedance versus *v* cross-plot for the selected location (Figs. 6 and 7). A yellow cluster has been added to this scatter plot compared to previous cross-plots. Therefore, it can be concluded that it has a somewhat better resolution than the previous two scatter plots. This new cluster contains dark red dots (The least depth) and is attributed to gas-bearing sand.

Table 5 - Geomechanical specifications according to Fig. 10.

Geomechanical specifications according to Fig. 10			
Geology/Fluid content	**Z_P (m/s) × (g/cc)**	**v Unit less**	**Colour of dots**
Shale	10000-12800	0.21-0.32	Blue - purple
Brine sand	7200-10000	0.18-0.28	Green - blue
Oil sand	5800-7200	0.16-0.25	Orange - green
Gas sand	4000-5200	0.11-0.23	Red

5.3.4. *MR* versus *LR* (*LMR*)

As previously discussed, λ is a function of both compression and shear properties of a material, whereas μ is purely a function of shear properties. As m is dependent on shear properties it is largely fluid-independent. This brings advantages when cross-plotting in *LMR* space as one axis remains fluid independently, unlike in conventional domains such as V_P/V_S versus P-impedance, where both axes are impacted by pore fluids (Close *et al*., 2015). *MR* gives a good separation between sand and shale and, hence, can serve as a good lithology discriminator in the seismic study field. High *MR* and low *LR* values define brine sand, whereas high *MR* and very low *LR* values correspond to hydrocarbon-bearing sands. The *LMR* cross-plot was plotted and clustered according to the above description and can be seen in Fig. 11. This scatter plot is one of the most useful cross-plots, therefore, we design different combinations of *LMR* cross-plots and perform more detailed studies.

For this purpose, we plot three-component cross-plots. In conventional cross-plots, the colour bar indicates time or depth. But in this type of three-component cross-plot, we use ERho ($E'\rho$) and Z_P for the colour of the dots. The results are shown in Figs. 12 and 13, respectively. In Fig. 12, where the colour of the dots indicates the amount of ERho, the red to yellow dots are in the hydrocarbon range, the yellow to green dots are in the brine sand range, and the light blue

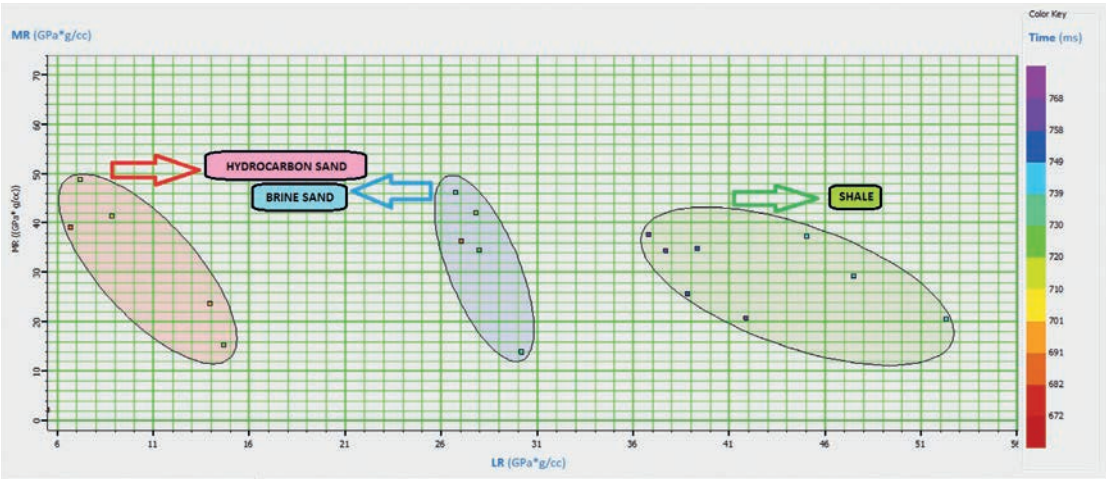

Fig. 11 - *LMR* cross-plot for the selected location (Figs. 6 and 7). The red cluster (hydrocarbon sand) and blue cluster (brine sand) have almost the same value as *MR*. The green cluster (shale) has less value. It can therefore be concluded that the amount of *MR* is independent of the type of fluid inside the pores and can be used to separate shale and sand.

to purple dots are in the shale range. It can thus be concluded that hydrocarbon ranges have the lowest ERho values following previous findings, and thus these areas can be identified well.

Similarly, in Fig. 13, the colour of the dots indicates the Z_P. Also, in this case, the lowest Z_P values are in the hydrocarbon range. Colour separation in this figure is better than in Fig. 12, and in this regard, the Z_P can be a better tool for separating hydrocarbon-bearing locations. Geomechanical specifications according to Figs. 11, 12, and 13 are shown in Table 6.

Table 6 - Geomechanical specifications according to Figs. 11, 12, and 13.

Geomechanical specifications according to Figs. 11, 12, and 13			
Geology/Fluid content	***MR*** **GP × (g/cc)**	***LR*** **Gpa × (g/cc)**	**Colour of dots**
Shale	20-40	36-52	It depends on the colour-bar parameter
Brine sand	14-50	14-50	
Hydrocarbon sand	14-50	7-15	

5.3.5. *MR/LR* versus *LR*

As shown in Figs. 11 to 13, in those cross-plots, *LR* makes a good distinction between shale and sand, as well as between hydrocarbon and brine. But the *MR* values are close and, therefore, have a low resolution (*MR* is not a fluid indicator). So, we designed a new parameter that has more resolution for fluid detection. This new parameter is the result of dividing *MR* by *LR*.

According to Table 1, the presence of shale will be associated with the maximum amount of *MR* and the minimum *LR*, so the product of dividing *MR* by *LR* for shale will have a minimum value and this ratio will increase for brine, oil-sand, and gas-sand, respectively. With this idea, the

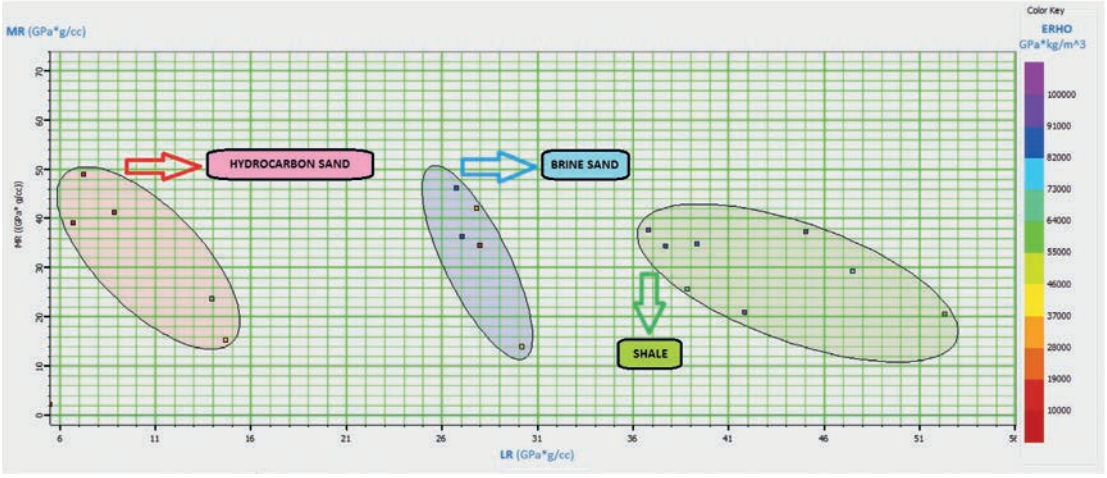

Fig. 12 - *LMR* colour bar and ERho cross-plot for the selected location (Figs. 6 and 7). This is a three-component scatter plot. The difference with the previous scatter plot is that the colour of the dots indicates the value of ERho instead of time or depth. Therefore, considering that the value of ERho for shale is greater than brine sand and hydrocarbon sand respectively, this third component can be used as a criterion for scatter plot validation. As can be seen, by changing the colour of the clusters from red to green (hydrocarbon to shale), the colour of the dots changes from red to dark blue and purple, which indicates an increase in the amount of ERho and shows the accuracy of the clustering.

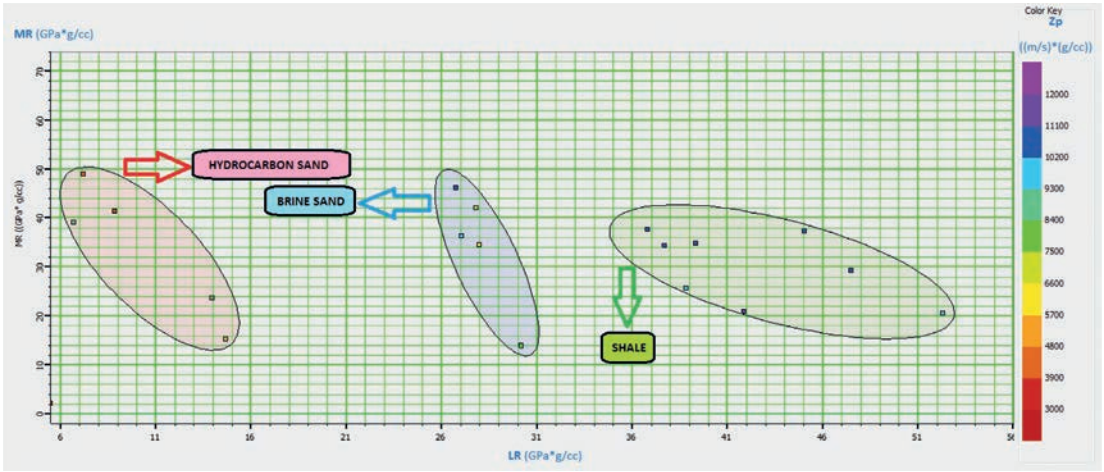

Fig. 13 - *LMR* colour bar: P-impedance cross-plot for the selected location (Figs. 6 and 7). This is a three-component scatter plot. Here, the P-impedance is considered the third component. It is known that the P-impedance for shale is higher than brine sand and hydrocarbon sand, respectively. This difference was used to validate the scatter plot. According to this figure, the colour of the ellipses varies from red (less P-impedance values) to dark blue and purple (more P-impedance values) as the cluster colour shifts from red to green (hydrocarbon to shale). Therefore, by increasing the Z_p values, the hydrocarbon area moves to shale, which is the theoretical reality and this issue can help to validate the scatter plot.

cross-plot for *MR*/*LR* versus *LR* was plotted and is shown in Fig. 14. As can be seen, the separation with this parameter is so good that the gas hydrocarbon (yellow cluster) is also singled out. In terms of depth, clustering is also compatible with geology. Hence, the red dots (lowest depth) are in the gas hydrocarbon range, the yellow, orange, and green dots (more depth) are in the oil and brine range, and the dark blue and purple dots (maximum depth) are in the shale range. Due to the importance of this scatter diagram, we plotted it in a wider range, which included 10

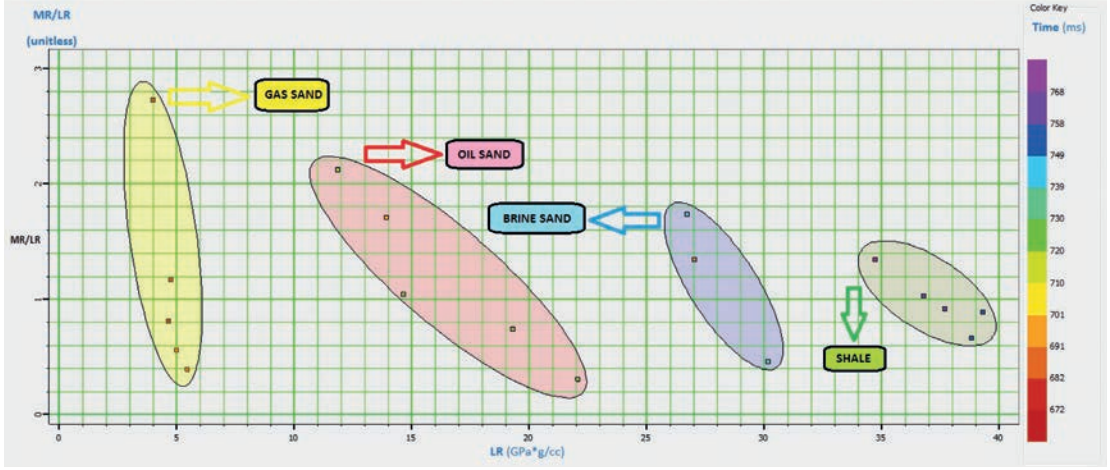

Fig. 14 - *MR*/*LR* versus *LR* cross-plot for the selected location (Figs. 6 and 7). This is probably the best scatter plot of the other scatter plots presented in this research. Because in addition to creating a good separation between shale and sand, it also provides the possibility of distinguishing between gas and oil. All of the dots are located inside the clusters and the distance between the clusters is such that it has a high resolution. The colour of the dots in the clusters changes from red to purple, respectively, indicating an increase in depth from gas hydrocarbon to shale.

in-lines and 10 cross-lines to the centre of the 'selected location'. The results are shown in Fig. 15. In this case, more than 90% of the dot symbols fall into distinct clusters. Therefore, it can be concluded that among all cross-plots drawn in this research, this cross-plot drawn with *MR*/*LR* parameter has the best results. Geomechanical specifications according to Figs. 14 and 15 are shown in Tables 7 and 8.

Table 7 - Geomechanical specifications according to Fig. 14.

Geomechanical specifications according to Fig. 14			
Geology/Fluid content	***MR/LR*** **Unit less**	***LR*** **GPa × (g/cc)**	**Colour of dots**
Shale	0.3-1.4	34-40	Dark blue - purple
Brine sand	0.2-1.8	26-30	Yellow - green
Oil sand	0.2-2.1	12-22	Orange - green
Gas sand	0.2-2.8	4.5-5.5	Red - orange

Table 8 - Geomechanical specifications according to Fig. 15.

Geomechanical specifications according to Fig. 15			
Geology/Fluid content	***MR/less*** **Unit less**	***LR*** **GPa × (g/cc)**	**Colour of dots**
Shale	0.4-1.8	17.5-24.5	Blue - purple
Brine sand	0.4-3	11-17	Green - dark blue
Oil sand	0.4-4	4.5-12	Orange - yellow - green
Gas sand	3.8-9	2-4.5	Red - orange

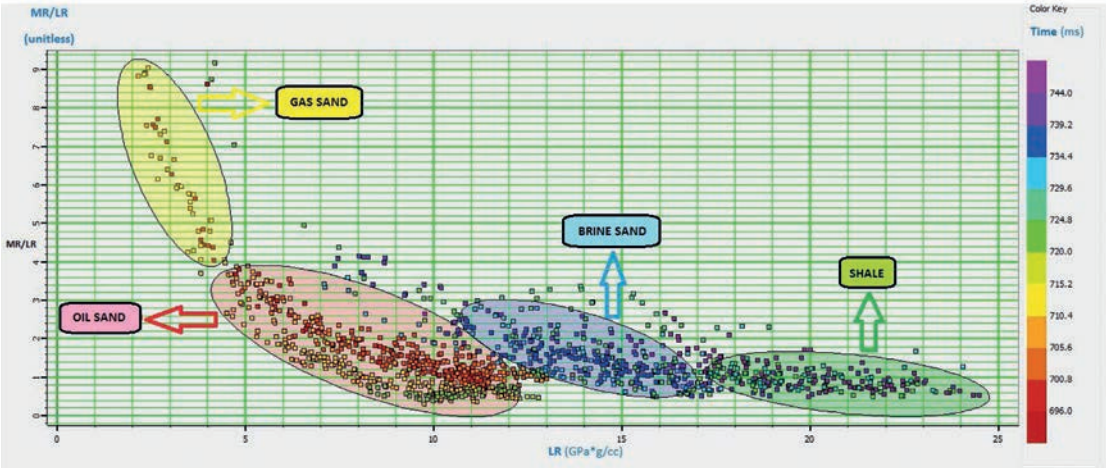

Fig. 15 - *MR*/V_s *LR* cross-plot. This scatter plot is provided for a range of 10 in-lines and 10 cross-lines to the centre of the 'selected location' indicated in Figs. 6 and 7. In this figure, by varying the colour of the dot symbols from red to purple, the time (depth) increases. The red-to-orange colour shows the gas sand cluster. The orange-to-green colour indicates the oil sand cluster. The light blue to dark blue colour indicates the brine sand cluster. The purple colour shows the shale cluster. Obviously, due to the expansion of data volume in this figure, some symbols do not fit inside the clusters. Note that more than 90% of the dot symbols fall into distinct clusters.

5.4. Validation

The obtained results were examined by plotting the P-impedance from simultaneous inversion versus existing wells' P-impedance log in a scatter plot. The choice of Z_p as a validation criterion is because this parameter is the basis for extracting other results and therefore it is a suitable option for validation. The result is shown in Fig. 16. According to this figure and regression line, the extracted Z_p has a correlation of 0.92016 with the data obtained from the existing well logs, which indicates the high accuracy of the outputs.

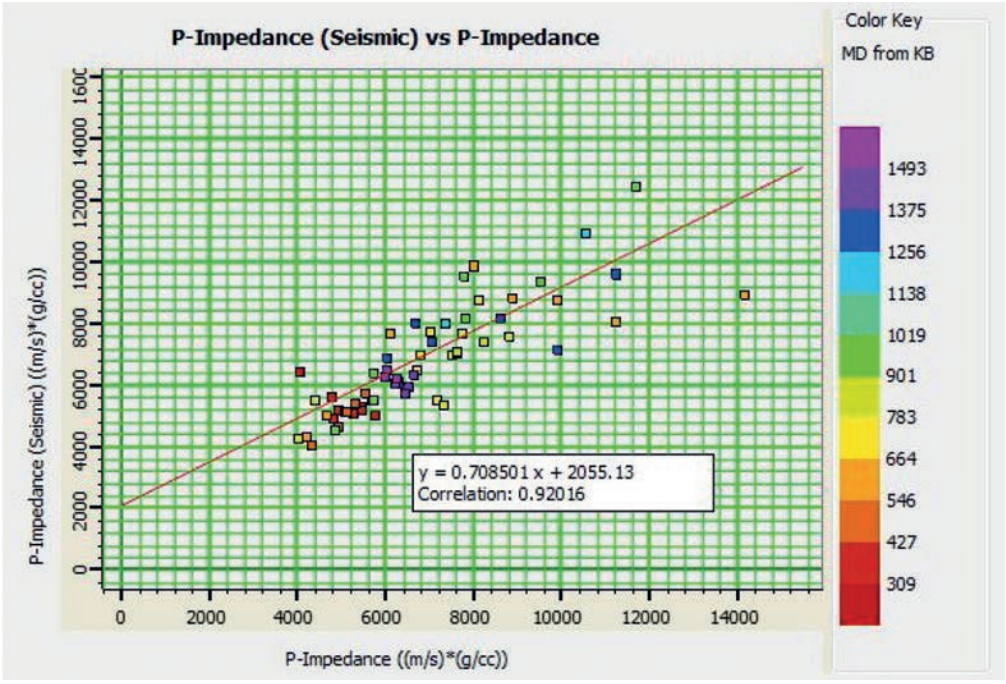

Fig. 16 - Inverted P-impedance versus Well A P-impedance cross-plot. The obtained dots have a correlation coefficient of 0.92016. The slope of the regression line is equal to 0.708501, which means that the angle of the regression line is approximately 35°. If the value of the inverted P-impedance and Well A-P impedance were the same, the regression line was plotted at a 45°-angle. Thus, there is only less than a 10° difference from the ideal state.

6. Conclusions

This present study was carried out to predict the higher hydrocarbon potential zones of a reservoir layer using 3D seismic data and integrated attributes in a two-step procedure. In addition, the shale zone of the reservoir is designated from hydrocarbon-bearing zones using scatter plots. An important point in this study is designing a detailed map to quickly evaluate the best locations of the reservoir in terms of hydrocarbon potential. This is particularly interesting because in most of the previous studies, the investigation of the reservoir requires the use of several well logs and multiple seismic sections, and evaluating them separately is complicated and time-consuming. We overcame this issue by using a multi-component 'horizontal slice' of the 'integrated attribute'. In a short period of time, we can therefore have an accurate evaluation of the hydrocarbon reservoir. On the other hand, we evaluated the location determined through

the horizontal slice vertically, using 5 scatter plots. All five cross-plots showed good results in separating shale from hydrocarbon, but some of them had more accurate results. We also solved the dots separation problem in scatter plots by using a two-step procedure. It is worth mentioning that the accuracy of this procedure is directly dependent on the accuracy of the inversion steps. In this regard, several wavelets and various velocity models were produced and subjected to inversion testing. The correlation of inversion in different modes varied from 0.79 to 0.92. Finally, the most accurate setting was chosen to carry out the inversion and to continue the study steps. Considering the results of the *MR*/*LR* versus *LR*, and Z_p versus *v* scatter plots, we found that this method is capable of properly distinguishing between brine, oil, and gas-bearing intervals. The validity of the method is verified by comparing our results and the existing information from the four wells. Our method is used to investigate the reservoir layer both laterally and vertically for evaluating the zones with higher hydrocarbon potential before the drilling operation and field development plan. There is a trade-off between the reservoir layer's maximum thickness and the "integrated attribute's" minimum value. We selected a balance between these values qualitatively, using horizontal slices.

7. Future developments for this study

We suggest analysing the trade-off between the maximum thickness of the reservoir layer and the minimum value of the 'integrated attribute' mathematically for faster implementations in future studies. Also analysing the results using a genetic algorithm attached to neural networks, can make this procedure faster and more accurate. It is also suggested to conduct more studies on the parameter proposed in this study *MR*/*LR*, versus other geomechanical parameters in scatter plots to check its efficiency.

Acknowledgments. The authors would like to acknowledge the Research Council of the University of Tehran. This research did not receive any specific grant from funding agencies in the public, commercial, or not-for-profit sectors.

REFERENCES

Adeoti L., Adesanya O.Y., Oyedele K.F., Afinotan I.P. and Adekanle A.; 2018: *Lithology and fluid prediction from simultaneous seismic inversion over Sandfish field, Niger Delta, Nigeria*. Geosci. J., 22, 155-169, doi: 10.1007/s12303-017-0018-4.

Adesanya O.Y., Adeoti L., Oyedele K.F., Afinotan I.P., Oyeniran T. and Alli S.; 2021: *Hydrocarbon reservoir delineation using simultaneous and elastic impedance inversions in a Niger Delta field.* J. Pet. Explor. Prod. Technol., 11, 2891-2904.

Aki K. and Richards P.G.; 1980: *Quantitative seismology: theory and methods, Vol. 1.* W.H. Freeman and Company, San Francisco, CA, USA, 557 pp.

Akram J. and Eaton D.W.; 2016: *Review and appraisal of arrival-time picking methods for downhole microseismic data*. Geophys., 81, KS71-KS91, doi: 10.1190/geo2014-0500.1.

Alsharhan A.S. and Nairn A.E.M.; 1997: *Sedimentary basins and petroleum of the Middle East*. Elsevier, Amsterdam, The Netherlands, 942 pp., doi: 10.1016/B978-0-444-82465-3.X5000-1.

Bagheri H., Tanha A.A., Doulati Ardejani F., Heydari-Tajareh M. and Larki E.; 2021: *Geomechanical model and wellbore stability analysis utilizing acoustic impedance and reflection coefficient in a carbonate reservoir*. J. Pet. Explor. Prod. Technol., 11, 3935-3961, doi: 10.1007/s13202-021-01291-2.

Bathellier E., Downton J. and Sena A.; 2012: *Optimizing CSG development: quantitative estimation of lithological and geomechanical reservoir quality parameters from seismic data*. In: Extended Abstracts 22nd International Geophysical Conference and Exhibition, ASEG 2012, Brisbane, Australia, pp. 1-4, doi: 10.1071/ASEG2012ab151.

Bjorlykke K., Hoeg K. and Mondol N.H.; 2015: *Introduction to Geomechanics: stress and strain in sedimentary basins*. In: Petroleum Geoscience - From Sedimentary Environemnts to Rock Physics, Springer-Verlag, Berlin Heidelberg, Germany, pp. 281-298, doi: 10.1007/978-3-642-02332-3_11.

Castagna J.P. and Swan H.W.; 1997: *Principle of AVO cross plotting*. The Leading Edge, 6, 337-344, doi: 10.1190/1.1437626.

Close D., Taylor R. and Nixon S.; 2015: *Rock physics and quantitative interpretation using Lambda-Mu-Rho in the Shipwreck Trough, Otway Basin*. In: Extended Abstracts, 24th International Geophysical Conference and Exhibition, ASEG 2015, Perth, Australia, pp. 1-4, doi: 10.1071/ASEG2015ab074.

Coppens F.; 1985: *First arrival picking on common-offset trace collections for automatic estimation of static corrections.* Geophys. Prospect., 33, 1212-1231, doi: 10.1111/j.1365-2478.1985.tb01360.x.

Das B. and Chatterjee R.; 2017: *Wellbore stability analysis and prediction of minimum mud weight for few wells in Krishna-Godavari Basin, India.* Int. J. Rock Mech. Min. Sci., 93, 30-37, doi: 10.1016/j.ijrmms.2016.12.018.

Das B. and Chatterjee R.; 2018: *Mapping of pore pressure, in situ stress, and brittleness in unconventional shale reservoir of Krishna-Godavari Basin*. J. Nat. Gas Sci. Eng., 50, 74-89.

Datta Gupta S., Chatterjee R. and Farooqui M.Y.; 2012: *Rock physics template (RPT) analysis of well-logs and seismic data for lithology and fluid classification in Cambay Basin*. Int. J. Earth Sci., 101, 1407-1426, doi: 10.1007/s00531-011-0736-1.

Faraji M.A., Kadkhodaie A., Rezaee R. and Wood D.A.; 2017: *Integration of core data, well logs, and seismic attributes for identification of the low reservoir quality units with unswept gas in the carbonate rocks of the world's largest gas field.* J. Earth Sci., 28, 857-866, doi: 10.1007/s12583-017-0800-2.

Fjær E., Holt R.M., Horsrud P., Raaen A. and Risnes R.; 2008: *Petroleum-related rock mechanics, 2nd ed*. Elsevier, Amsterdam, The Netherlands, 491 pp.

Goodway B.; 2001: *A tutorial on AVO and Lamé constants for rock parameterization and fluid detection.* <https://www.academia.edu/6369293/A_tutorial_on_AVO_and_Lamé_constants_for_rock_parameterization_and_fluid_detection>.

Goodway W., Chen T. and Downton J.; 1997: *Improved AVO fluid detection and lithology discrimination using lame petrophysical parameters; "λρ","μρ",&"λ/μ fluid stack", from P and S inversions.* In: Expanded Abstracts, 67th Annual International Meeting, SEG Technical Program, Denver, CO, USA, pp. 183-186, doi: 10.1190/1.1885795.

Guo S. and Wang H.; 2019: *Seismic absolute acoustic impedance inversion with L1 norm reflectivity constraint and combined first and second-order total variation regularizations*. J. Geophys. Eng., 16, 773-788, doi: 10.1093/jge/gxz048.

Hackert C.L. and Parra J.O.; 2002: *Calibrating well logs to VSP attributes: interval velocity and amplitude.* The Leading Edge, 21, 52-57, doi: 10.1190/1.1445848.

Han Y., Liu C., Phan D., AlRuwaili K. and Abousleiman Y.; 2019: *Advanced wellbore stability analysis for drilling naturally fractured rocks*. In: Proc. Middle East Oil and Gas Show and Conference, Society of Petroleum Engineers, Manama, Bahrain, SPE-195021-MS, 18 pp., doi: 10.2118/195021-MS.

Hoseinpour M. and Riahi M.A.; 2021: *Determination of the mud weight window, optimum drilling trajectory, and wellbore stability using geomechanical parameters in one of the Iranian hydrocarbon reservoirs.* Journal of Petroleum Exploration and Production Technology, 12, 83-82.

James G.A. and Wynd J.G.; 1965: *Stratigraphic nomenclature of Iranian Oil Consortium agreement area1*. AAPG Bull., 49, 2182-2245, doi: 10.1306/A663388A-16C0-11D7-8645000102C1865D.

Kadkhodaie-Ilkhchi A., Monteiro S.T., Ramos F. and Hatherly P.; 2010: *Rock recognition from MWD data: a comparative study of boosting, neural networks, and fuzzy logic*. IEEE Geosci. Remote Sens. Lett., 7, 680-684, doi: 10.1109/LGRS.2010.2046312.

Kassem A.A., Sen S., Radwan A.E., Abdelghany W.K. and Abioui M.; 2021: *Effect of depletion and fluid injection in the Mesozoic and paleozoic sandstone reservoirs of the October oil field, central Gulf of Suez Basin: implications on drilling, production and reservoir stability.* Nat. Resour. Res., 30, 2587-2606.

Khaitan M.L., Ranjan P., Chandrasekhar S. and Kumar B.; 2017: *Utilizing the uniqueness of Vertical Seismic Profiling (VSP) for deepwater exploration.* In: Proc. 4th Borehole Geophysics Workshop, European Association of Geoscientists & Engineers, Abu Dhabi, United Arab Emirates, pp. 1-5, doi: 10.3997/2214-4609.201702486.

Khatibi S., Aghajanpour A., Ostadhassan M. and Farzay O.; 2018: *Evaluating single-parameter parabolic failure criterion in wellbore stability analysis*. J. Nat. Gas Sci. Eng., 50, 166-180, doi: 10.1016/j.jngse.2017.12.005.

Khoshnevis-zadeh R., Soleimani B. and Larki E.; 2019: *Using drilling data to compare geomechanical parameters with porosity (a case study, South Pars gas field, south of Iran).* Arab. J. Geosci., 12, 1-10, doi: 10.1007/s12517-019-4809-y.

Kong L., Ostadhassan M., Zamiran S., Liu B., Li C. and Marino G.G; 2019: *Geomechanical upscaling methods: comparison and verification via 3D printing*. Energies, 12, 382, doi: 10.3390/en12030382.

Koop W.J. and Stoneley R.; 1982: *Subsidence history of the middle east Zagros Basin, Permian to recent.* Philos. Trans. R. Soc. London, Ser. A, 305, 149-168, doi: 10.1098/rsta.1982.0031.

Krebs J.R., Anderson J.E., Hinkley D., Neelamani R., Lee S., Baumstein A. and Lacasse M.D.; 2009: *Fast full-wave field seismic inversion using encoded sources*. Geophys., 74, WCC177-WCC188, doi: 10.1190/1.3230502.

Larki E., Tanha A.A., Parizad A., Soltani Soulgani B. and Bagheri H.; 2021: *Investigation of quality factor frequency content in vertical seismic profile for gas reservoirs*. Pet. Res., 6, 57-65, doi: 10.1016/j.ptlrs.2020.10.002.

Larki E., Dehghani A.H.S. and Tanha A.A.; 2022: *Investigation of geomechanical characteristics in one of the Iranian oilfields by using vertical seismic profile (VSP) data to predict hydraulic fracturing intervals*. Geomec. Geophys. Geo-energ. Geo-resour., 8, 1-23, doi: 10.1007/s40948-022-00365-7.

Li S., Peng Z. and Wu H.; 2018: *Prestack multi-gather simultaneous inversion of elastic parameters using multiple regularization constraints*. J. Earth Sci., 29, 1359-1371.

Lu X., Zhao M., Liu K., Zhuo Q., Fan J., Yu Z. and Gong Y.; 2018: *Formation condition of deep gas reservoirs in tight sandstones in Kuqa Foreland Basin*. Pet. Res., 3, 346-358, doi: 10.1016/j.ptlrs.2018.11.003.

Mandal A. and Ghosh S.K.; 2020: *Estimating broad trend of acoustic impedance profile from observed seismic reflection data using first principles only.* J. Geophys. Eng., 17, 475-483, doi: 10.1093/jge/gxaa006.

Matsushima J., Ali M.Y. and Bouchaala F.; 2016: *Seismic attenuation estimation from zero-offset VSP data using seismic interferometry.* Geophys. J. Int., 204, 1288-1307.

McCormack M.D., Zaucha D.E. and Dushek D.W.; 1993: *First-break refraction event picking and seismic data trace editing using neural networks*. Geophys., 58, 67-78.

Molyneux J.B. and Schmitt D.R.; 1999: *First-break timing: arrival onset times by direct correlation*. Geophys., 64, 1492-1501.

Morozov I.B. and Ma J.; 2009: *Accurate post-stack acoustic-impedance inversion by well-log calibration*. Geophys., 74, R59-R67, doi: 10.1190/1.3170687.

Na'imi S.R., Shadizadeh S.R., Riahi M.A. and Mirzakhanian M.; 2014: *Estimation of reservoir porosity and water saturation based on seismic attributes using support vector regression approach*. J. Appl. Geophys., 107, 93-101, doi: 10.1016/j.jappgeo.2014.05.011.

Nakaten N., Schlüter R., Azzam R. and Kempka T.; 2014: *Development of a techno-economic model for dynamic calculation of the cost of electricity, energy demand and CO2 emissions of an integrated UCG-CCS process*. Energy, 66, 779-790, doi: 10.1016/j.energy.2014.01.014.

Ogbamikhumi A. and Igbinigie N.S.; 2020: *Rock physics attribute analysis for hydrocarbon prospectivity to the Eva field onshore Niger Delta Basin*. J. Pet. Explor. Prod. Technol., 10, 3127-3138, doi: 10.1007/s13202-020-00975-5.

Omudu L.M. and Ebeniro J.O.; 2005: *Cross-plotting of rock properties for fluid discrimination using well data in offshore Niger Delta*. Niger. J. Phys., 17, 16-20, doi: 10.4314/njphy.v17i1.37986.

Pan S., Qin Z., Lan H. and Badal J.; 2019: *Automatic first-arrival picking method based on an image connectivity algorithm and multiple time windows*. Comput. Geosci., 123, 95-102, doi: 10.1016/j.cageo.2018.12.001.

Pelletier H.; 2009: *AVO Crossplotting II: examining Vp/Vs behavior*. CSPG, CSEG, CWLS Convention, Calgary, Alberta, Canada, pp. 105-110.

Perez R.; 2010: *Application of LMR inversion and clustering analysis in the Barnett Shale*. In: Expanded Abstracts, 80th Annual International Meeting, SEG, Denver, CO, USA, pp. 2236-2239.

Perez R.; 2011: *Application of LMR and clustering analysis in unconventional reservoirs*. Presented at AAPG Geoscience Technology Workshop, International Shale Plays, Houston, TX, USA.

Radwan A.E. and Sen S.; 2021: *Stress path analysis for characterization of in situ stress state and effect of reservoir depletion on present-day stress magnitudes: reservoir geomechanical modeling in the Gulf of Suez Rift Basin, Egypt*. Nat. Resour. Res., 30, 463-478.

Radwan A.E., Abudeif A.M., Attia M.M. and Mohammed M.A.; 2019: *Pore and fracture pressure modeling using direct and indirect methods in Badri field, Gulf of Suez, Egypt*. J. Afr. Earth Sci., 156, 133-143, doi: 10.1016/j.jafrearsci.2019.04.015.

Radwan A.E., Abudeif A.M., Attia M.M., Elkhawaga M.A., Abdelghany W.K. and Kasem A.A.; 2020: *Geopressure evaluation using integrated basin modeling, well-logging, and reservoir data analysis in the northern part of the Badri oil field, Gulf of Suez, Egypt*. J. Afr. Earth Sci., 162, 103743, doi: 10.1016/j.jafrearsci.2019.103743.

Radwan A.E., Abdelghany W.K. and Elkhawaga M.A.; 2021: *Present-day in-situ stresses in southern Gulf of Suez, Egypt: insights for stress rotation in an extensional rift basin*. J. Struct. Geol., 147, 104334, doi: 10.1016/j.jsg.2021.104334.

Rutqvist J., Vasco D. and Myer L.; 2009: *Coupled reservoir-geomechanical analysis of CO_2 injection and ground deformations at In Salah, Algeria.* International Journal of Greenhouse Gas Control, 4, 225-230, doi: 10.1016/j.ijggc.2009.10.017.

Schön J.H.; 2015: *Physical properties of rocks: fundamentals and principles of petrophysics, 2nd ed*. Elsevier, Amsterdam, The Netherlands, 512 pp.

Sengupta M., Dai J., Volterrani S., Dutta N., Rao N.S., Al-Qadeeri B. and Kidambi V.K.; 2011: *Building a seismic-driven 3D geomechanical model in a deep carbonate reservoir*. In: Expanded Abstracts, 81st Annual Meeting, SEG Technical Program, S. Antonio, TX, USA, pp. 2069-2073, doi: 10.1190/1.3627616.

Shahbazi K., Zarei A.H., Shahbazi A. and Tanha A.A.; 2020: *Investigation of production depletion rate effect on the near-wellbore stresses in the two Iranian southwest oilfields*. Pet. Res., 5, 347-361.

Sharma R. and Chopra S.; 2012: *New attribute for determination of lithology and brittleness*. In: Expanded Abstracts, 82nd Annual Meeting, SEG Technical Program, Las Vegas, NV, USA, pp. 1-5, doi: 10.1190/SEGAM2012-1389.1.

Shuaib M.E.K. and Berguig M.C.; 2022: *Thin-bed reservoir characterization by integration of seismic inversion, multi attributes analysis and neural network: a case study in the Sufyan oil field of the Muglad rift basin, Sudan*. Bull. Geoph. Ocean., 63, 455-480.

Soleimani B., Rangzan K., Larki E., Shirali K. and Soleimani M.; 2018: *Gaseous reservoir horizons determination via Vp/Vs and Q-Factor data, Kangan-Dalan Formations, in one of SW Iranian hydrocarbon fields*. Geopersia, 8, 61-76, doi: 10.22059/geope.2017.239616.648340.

Suslick S.B., Schiozer D. and Rodriguez M.R.; 2009: *Uncertainty and risk analysis in petroleum exploration production*. Terrae, 6, 30-41.

Ujuanbi O., Okolie J.C. and Jegede S.I.; 2008: *Lambda-Mu-Rho techniques as a viable tool for litho-fluid discrimination - the Niger - Delta example*. Int. J. Phys. Sci., 3, 173-176, doi: 10.5897/IJPS.9000342.

Wu X., Willis M.E., Palacios W., Ellmauthaler A., Barrios O., Shaw S. and Quinn D.; 2017: *Compressional- and shear-wave studies of distributed acoustic sensing acquired vertical seismic profile data*. The Leading Edge, 36, 987-993, doi: 10.1190/tle36120987.1.

Yang J., Zong J., Li Y.E. and Cheng A.; 2020: *Application of reverse time migration with random space shift to Vertical Seismic Profiling (VSP) data*. In: Proc. EAGE Annual Conference & Exhibition Online, European Association of Geoscientists & Engineers, pp. 1-5, doi: 10.3997/2214-4609.202011498.

Yasin Q., Sohail G.M., Ding Y., Ismail A. and Du Q.; 2020: *Estimation of petrophysical parameters from seismic inversion by combining particle swarm optimization and multilayer linear calculator*. Nat. Resour. Res., 29, 3291-3317.

Zoback M.D.; 2007: *Reservoir Geomechanics*. Cambridge University Press, Cambridge, UK, 452 pp., doi: 10.1017/CBO9780511586477.

Corresponding author: Mohammad Ali Riahi
Institute of Geophysics, University of Tehran
Kangar Ave., Tehran, Iran
Phone: +98 21 61118219; e-mail: mariahi@ut.ac.ir